Journal of
Materials Chemistry A

PAPER

View Article Online
View Journal | View Issue

Cite this: *J. Mater. Chem. A*, 2024, **12**, 33799

Scalable synthesis of N-doped graphene-oxide-supported FeCo(OH)$_x$ nanosheets for efficient Co-doped Fe$_3$O$_4$ nanoparticle-based oxygen reduction reaction electrocatalysis†

Sunglun Kwon and Jong Hyeon Lee *

Received 19th September 2024
Accepted 10th November 2024

DOI: 10.1039/d4ta06684g

rsc.li/materials-a

Developing efficient and cost-effective materials is crucial for advancing the electrochemical oxygen reduction reaction (ORR). By introducing Co^{2+} ions into formamide, our method prevents rapid Fe^{2+} oxidation to Fe^{3+}, promoting the formation of well-defined Fe$_3$O$_4$ nanoparticles rather than Fe$_2$O$_3$. This study presents a synthesis route for high-performance spinel Fe and Co oxide nanoparticles on N-doped reduced graphene oxide (NRGO). This solvothermal synthesis in formamide yields well-dispersed, ultrafine FeCo(OH)$_x$ nanoparticles (~5 nm) anchored on NRGO. These nanoparticles can be employed for the formation of spinel Fe$_x$Co$_{3-x}$O$_4$ oxide nanoparticles, potentially due to their high surface area and strong interaction with the NRGO support. This, in turn, facilitates the successful decoration of highly dispersed spinel Fe$_x$Co$_{3-x}$O$_4$ oxide nanoparticles (~30 nm) onto the NRGO support, even after calcination at 900 °C, which represents the critical temperature for conventional graphitization. This unique approach results in significantly reduced particle aggregation compared with that of conventional methods. The (Co)Fe$_3$O$_4$-NRGO nanocomposite exhibits remarkable ORR activity, achieving an electron number of ~3.7 and a current density of 5.01 mA cm^{-2} at E = 0.75 V$_{RHE}$, comparable to those of commercial Pt/C catalysts. Furthermore, the catalyst exhibits remarkable stability, maintaining a reducing current density that is 42% lower after 40 000 s of uninterrupted operation at 0.75 V$_{RHE}$ compared with a 75% reduction observed with Pt/C. This exceptional performance is attributed to the strong interaction between the (Co)Fe$_3$O$_4$ nanoparticles and NRGO, facilitated by the Co ion precursor during annealing.

Introduction

The increasing demand for clean-energy technology, particularly fuel cells, has created a growing need for low-cost, high-performance transition metal catalysts for the oxygen reduction reaction (ORR).[1–5] The advancement of the electrochemical ORR relies on the development of materials that are both efficient and low-cost, as they can address crucial environmental problems.[5–9] ORR electrocatalysis is important in fuel cell cathodes, spurring significant research efforts to address its limitations and enhance fuel cell efficiency and stability.[10,11] ORR catalysis based on platinum-group metals is widely employed; however, the high cost and poor durability of the metals hinder their practical applications.[9,11–14]

Transition metal oxides, particularly spinel Co$_3$O$_4$ and its inverse spinel counterpart Fe$_3$O$_4$, have emerged as attractive alternatives to Pt/C catalysts for the ORR because of their cost-effectiveness, inherent activity, and superior resistance to particle aggregation, compared with Pt/C.[15,16] Notably, Fe$_3$O$_4$ offers advantages over Co$_3$O$_4$ because of its earth abundance.[17,18] However, achieving high ORR performance with Fe$_3$O$_4$ necessitates careful control of its structure and morphology.[19,20] Crystalline Fe$_3$O$_4$ nanoparticles with a single phase are crucial for maximizing active sites, whereas small particle sizes enhance surface area and mass transport.[19–22]

To address these limitations and unlock the full potential of Fe$_3$O$_4$ for the ORR, we propose a synthetic approach based on intermediate control. This method involves the transformation of layered double hydroxide (LDH)-like Fe(OH)$_x$ intermediates into well-dispersed, nanosized Fe(OH)$_x$ species anchored on N-doped reduced graphene oxide (NRGO). This approach leverages our previously demonstrated control over intermediate hydroxide species.[1] In our prior work, Co(OH)$_2$ single layers were employed to successfully decorate RGO, affording well-dispersed Co$_3$O$_4$ nanoparticles, approximately 5 nm in size.[1] This established method offers a promising strategy for synthesizing spinel nanoparticles, such as Fe$_3$O$_4$, while preventing particle aggregation even at high calcination temperatures.

Department of Chemistry, The Catholic University of Korea, Bucheon, 14662, Korea. E-mail: jhlee305@catholic.ac.kr

† Electronic supplementary information (ESI) available: XRD, photos, SEM, TEM, elemental maps, XPS data, ORR data, and K–L plots of (Co)Fe$_3$O$_4$–NRGO. See DOI: **https://doi.org/10.1039/d4ta06684g**

In conventional Fe_3O_4 nanoparticle synthesis, undesirable byproducts may form when carried out in organic or aqueous media, such as Prussian blue in the presence of CN^- ions and α-Fe_2O_3 in environments with excess O_2.[23–25] To overcome these limitations and create precisely defined nanoparticles, this study uses the intermediate control method. Through this process, ultra-small $FeCo(OH)_x$ intermediate nanoparticles are carefully grown on NRGO. This intermediate phase not only supports the uniform distribution of nanoparticles but also minimizes particle agglomeration, ensuring a stable and well-dispersed catalyst structure. This approach offers several advantages: (1) the prevention of particle aggregation during high-temperature calcination, (2) the enhancement of ORR electrocatalytic performance, (3) the improvement of crystallinity and single-phase magnetite formation, and (4) the production of well-defined, small particles on the conducting layer even at elevated temperatures (up to 900 °C). Additionally, the incorporation of Co precursors simplifies the process by eliminating the need for a separate hydroxide synthesis step and effectively prevents particle aggregation.

We introduce a solvothermal treatment to prepare LDH-like $FeCo(OH)_x$ nanosheets on NRGO. Subsequent calcination at 900 °C, the critical temperature for conventional graphitization, results in $(Co)Fe_3O_4$ spinel nanocrystals on highly graphitized NRGO supports. This optimized temperature enables the production of uniformly distributed spinel $(Co)Fe_3O_4$ nanoparticles (~30 nm) on the NRGO support.

Scheme 1 illustrates the synthesis process, including the formation of $FeCo(OH)_x$ nanosheets *via* the solvothermal reaction, their anchoring on NRGO, and their subsequent calcination to form $(Co)Fe_3O_4$ nanoparticles uniformly deposited on the NRGO. The Fe-only path introduces a mixture of Prussian blue and $Fe(OH)_3$, affording an irregular mixture of α-Fe_2O_3 and Fe_3O_4. In this work, the incorporation of Co^{2+} in the Fe^{2+} precursor solution leads to the formation of an ultrathin LDH-like $FeCo(OH)_x$ phase on the NRGO surface and the production of well-decorated spinel $(Co)Fe_3O_4$ on the NRGO sheet for ORR electrocatalysis.

Results and discussion

Role of Co ions in the formation of $(Co)Fe_3O_4$-NRGO

The X-ray diffraction (XRD) pattern of $(Co)Fe_3O_4$-NRGO (Fig. 1A) showed the successful formation of spinel $(Co)Fe_3O_4$ and the absence of peaks corresponding to α-Fe_2O_3. This suggested the successful inhibition of α-Fe_2O_3 formation during the calcination of $FeCo(OH)_x$ at 900 °C. The formation of intermediate hydroxides and their calcined products was characterized by XRD analysis. For comparison, a control group was prepared without the addition of Co ions, affording $Fe(OH)_3$ during the solvothermal synthesis. The characteristic peaks of $Fe(OH)_3$ were observed in the XRD pattern of $Fe(OH)_x$–NRGO, which corresponded to 17.4° and 34.8° (Fig. 1A). An additional broad peak at approximately 24.5° was attributed to the glass holder. The presence of NRGO was confirmed by the XRD peak at 43.2° (Fig. 1A, labeled NRGO). This peak suggested the presence of partially oxidized graphene sheets, likely due to the solvothermal or cleaning processes.

Following calcination, a new peak appeared, as shown in Fig. 1A (labeled G), corresponding to the characteristic diffraction peak (26.5°) of graphite. The XRD analysis of the $Fe(OH)_x$–NRGO composite after calcination at 900 °C revealed a transformation into a mixture of α-Fe_2O_3 and Fe_3O_4 phases. Additionally, the diffraction peaks corresponding to metallic iron were observed in both samples. While $Fe(OH)_3$ can be a precursor to α-Fe_2O_3 and Fe_3O_4 under specific conditions, it may decompose during the high-temperature calcination process (900 °C), resulting in a mixture of α-Fe_2O_3 (33.2°, 35.7°, 49.4°, 53.9°, and 62.5°) and Fe_3O_4 (30.4°, 35.7°, 43.2°, 57.1°, and 63.1°). The XRD patterns of α-Fe_2O_3 and Fe_3O_4, including

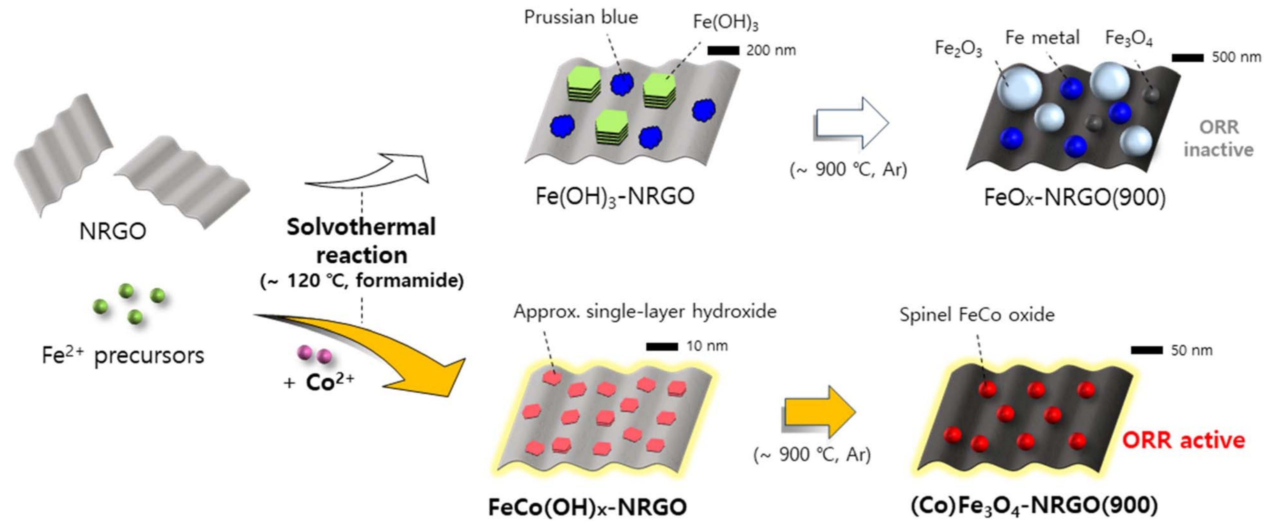

Scheme 1 Schematic illustration of $FeCo(OH)_x$ nanosheet precursor preparation and transformation into spinel $(Co)Fe_3O_4$ on a NRGO support. This approach offers a controlled synthesis route compared to conventional methods that often lead to a mixture of α-Fe_2O_3 and Fe_3O_4 during calcination of commercial magnetite.

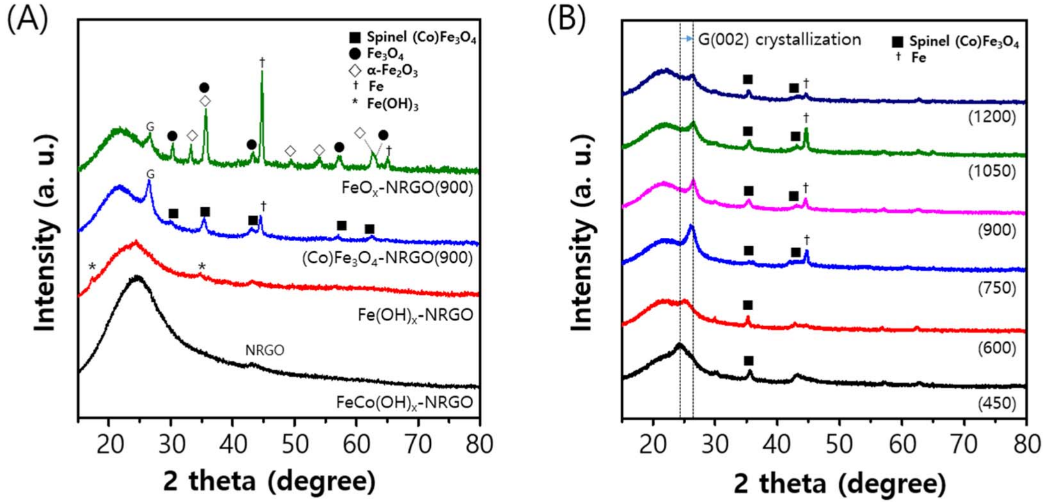

Fig. 1 XRD patterns of (A) FeCo(OH)$_x$–NRGO, Fe(OH)$_x$–NRGO, (Co)Fe$_3$O$_4$–NRGO (calcined at 900 °C), and FeO$_x$–NRGO (900). (B) (Co)Fe$_3$O$_4$–NRGO calcined at various temperatures (450–1200 °C). The inset specifies that G and GO represent graphite and graphene oxide, respectively.

reference data from the PDF file database, are provided in Fig. S1† for comparison. The FeCo(OH)$_x$–NRGO sample showed no diffraction peaks, except for the NRGO support before calcination. However, dominant peaks for the calcined forms of the (Co)Fe$_3$O$_4$ phases, 29.9°, 35.4°, 43.1°, 57.1°, and 62.4°, appeared along with weak diffraction signals for metallic iron (44.8° and 65.0°). The result indicated that Co influenced the formation of the FeCo(OH)$_x$ phase, potentially promoting the phase transition to the spinel (Co)Fe$_3$O$_4$ phase during calcination.

The synthesis of the spinel (Co)Fe$_3$O$_4$ nanoparticles was further supported by observations from the solvothermal reaction conducted without the NRGO support (Fig. S1†). Interestingly, the solvothermal reaction without the NRGO support did not yield any precipitate after 6 h; however, precipitation was observed after 12 h (Fig. S1A†). The transmission electron microscopy (TEM) image of the 6 h sample might suggest the presence of nanosheets within the colloidal solution, composed of Co–Fe hydroxide (Fig. S1B†). However, without Co, the solvothermal reaction afforded a predominant precipitate of α-Fe$_2$O$_3$ (Fig. S1C†). This observation suggested that the presence of Co caused the FeCo(OH)$_x$ nanosheet to suppress the formation of α-Fe$_2$O$_3$. The 12 h FeCo(OH)$_x$ sample, exhibiting initial powder formation, contained both Fe(OH)$_3$ and Prussian blue phases according to XRD (Fig. S1C†). After calcination at 900 °C, FeCo(OH)$_x$ transformed primarily into Fe$_3$O$_4$, as evidenced by the XRD result (Fig. 1). However, the presence of metallic iron likely stems from the partial reduction of iron oxides, a common side reaction during high-temperature calcination. Interestingly, commercially available Prussian blue also showed metallic iron phases after calcination at 900 °C (Fig. S2†), similar to our (Co)Fe$_3$O$_4$–NRGO and (Co)Fe$_3$O$_4$ samples (Fig. 1, S1, and S2†).

The XRD patterns of the FeCo(OH)$_x$-NRGO samples calcined at elevated temperatures revealed a shift in the (002) peak of the NRGO component (Fig. 1B, labeled G(002)). This peak shifted from 24.1° to 26.5° as the calcination temperature increased from 450 °C to 900 °C, indicating improved graphitization of the NRGO sheets. No further peak shift was observed above 900 °C, suggesting the completion of graphitization at 900 °C. Additionally, severe particle aggregation on the NRGO was observed at temperatures exceeding 1050 °C (Fig. S4†). Achieving highly crystalline nanoparticles often requires high crystallinity in the supporting graphene.[7,26] However, high-temperature treatments typically used for graphene synthesis can damage its crystalline structure.[27] These high temperatures can promote unwanted graphene-sheet breakdown, further affecting the crystallinity of the nanoparticles grown on them.[27,28] Importantly, the XRD patterns of all samples exhibited diffraction peaks corresponding solely to the (Co)Fe$_3$O$_4$ phase, and no peaks for α-Fe$_2$O$_3$ were detected. Therefore, this method offers a significant advantage in decorating crystalline spinel Fe$_3$O$_4$ nanocatalysis onto the highly graphitized NRGO support, affording high ORR activity due to the synergistic effect between the (Co)Fe$_3$O$_4$ nanoparticles and the conductive NRGO sheet.

Scanning electron microscopy (SEM), high-resolution TEM (HR-TEM), and scanning TEM were employed to investigate the morphology, size distribution, and elemental distribution of the as-prepared hydroxides and their corresponding calcined products (Fig. 2). Both Fe(OH)$_x$–NRGO and its calcined product at 900 °C showed large aggregates on the NRGO supports (Fig. S5†), probably due to fast aggregation of the Fe(OH)$_x$ phase during the solvothermal reaction. In contrast, FeCo(OH)$_x$–NRGO showed fine particles smaller than 10 nm on the NRGO surface. Notably, the calcined (Co)Fe$_3$O$_4$–NRGO exhibited well-dispersed nanoparticles. The SEM results of the FeCo(OH)$_x$–NRGO composite depicted the uniform dispersion of the FeCo(OH)$_x$ nanoparticles, averaging approximately 5 nm in size, anchored on the NRGO sheets (Fig. 2A–C). Upon calcination at 900 °C, these particles transformed into (Co)Fe$_3$O$_4$ nanoparticles, exhibiting an average size of 20.1 ± 5.8 nm, while maintaining excellent dispersion on the entire NRGO surface

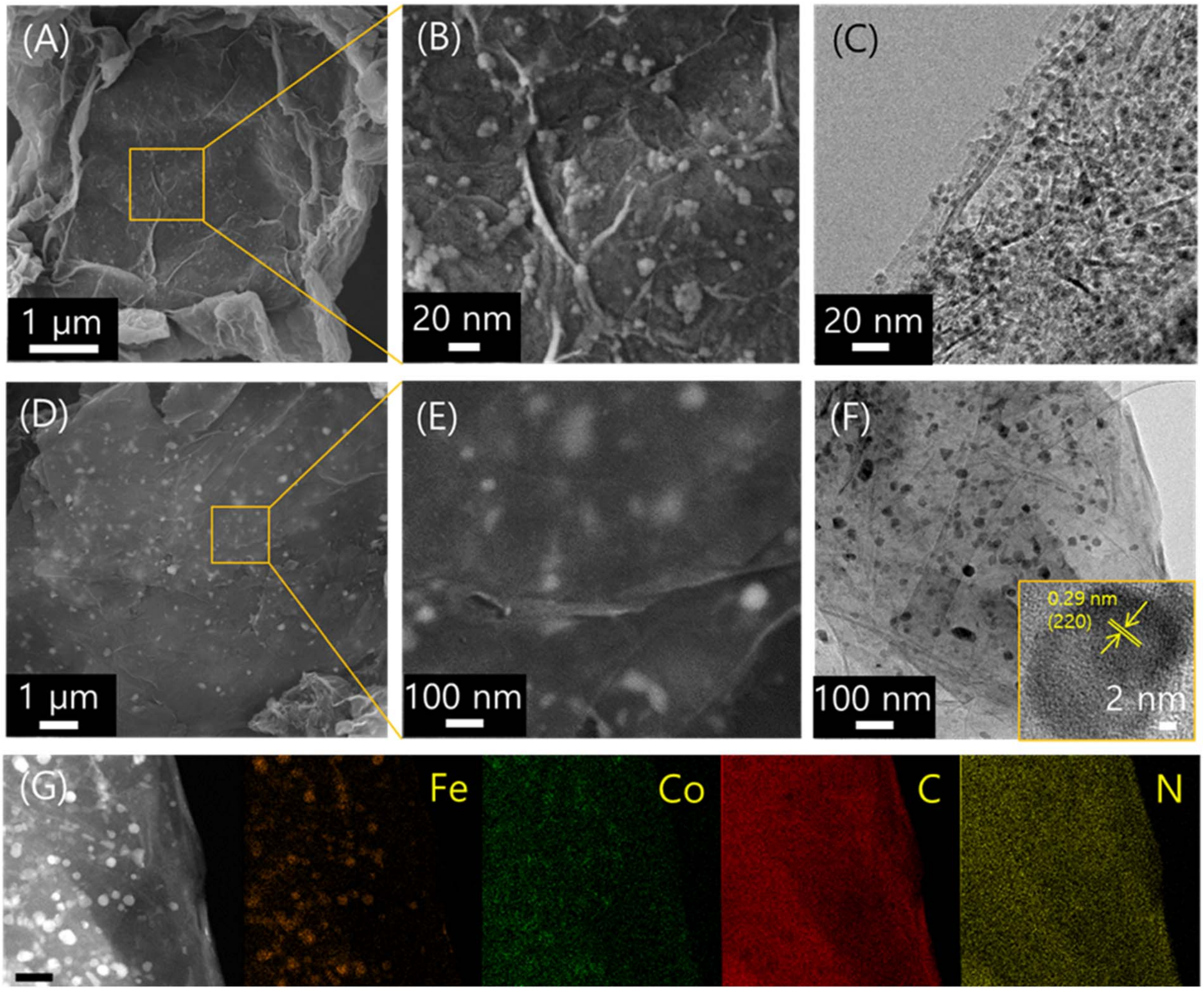

Fig. 2 (A–C) SEM and TEM images of FeCo(OH)$_x$—NRGO. (D–F) SEM and TEM images of Co(Fe$_3$O$_4$)–NRGO, and inset of (F) shows HR-TEM lattice images. (G) Scanning transmission electron microscopy (STEM) image of Co(Fe$_3$O$_4$)–NRGO with the corresponding elemental mapping images for Fe, Co, C and N (scale bar: 100 nm).

(Fig. 2D and E). Energy dispersive X-ray spectroscopy (EDS) validated the co-localization of Fe and Co within the (Co)Fe$_3$O$_4$ particles (Fig. 2G), indicating a well-defined mixed metal oxide.

X-ray photoelectron spectroscopy (XPS) was employed to analyze the atomic chemical composition of FeCo(OH)$_x$–NRGO and (Co)Fe$_3$O$_4$–NRGO, specifically focusing on investigating the Fe and Co species through the photoelectric effect (Fig. S6†). A comparison of the C 1s spectra between FeCo(OH)$_x$–NRGO and (Co)Fe$_3$O$_4$–NRGO (900 °C) revealed a pronounced disparity in the relative intensities of C═C and C–C peaks. Notably, (Co) Fe$_3$O$_4$–NRGO (900 °C) exhibited approximately 1.5 times higher intensity for these peaks, indicating a significant enhancement in NRGO crystallization. This observation was consistent with the calcination process, wherein the removal of oxygen and hydroxyl groups facilitated C–C bond formation.

Conversely, the intensities of the C–O and C═O peaks were approximately 4 times lower in (Co)Fe$_3$O$_4$–NRGO (900 °C) than in FeCo(OH)$_x$–NRGO, indicative of reduced oxygen functionalities (Fig. S6A†). The analysis of the Fe 2p$_{3/2}$ spectra provided insights into the oxidation states of iron in both FeCo(OH)$_x$–NRGO and (Co)Fe$_3$O$_4$–NRGO (900 °C). The presence of a peak at 709.9 eV in both samples confirmed the existence of Fe^{2+}, indicative of magnetite (Fe$_3$O$_4$) formation in the final products. Furthermore, the detection of Fe metal peaks at 707.5 and 708.4 eV in both samples suggested the coexistence of metallic iron, a finding corroborated by XRD patterns, which identified the presence of an iron metal phase (Fig. S6B†). O 1s analysis revealed a peak at 530.5 eV in both FeCo(OH)$_x$–NRGO and (Co) Fe$_3$O$_4$–NRGO (900 °C), confirming the presence of metal–oxygen bonding (Fig. S6C†). Co 2p analysis indicated weakly detected Co peaks at 795.0 eV in the Co 2p spectra of both FeCo(OH)$_x$–NRGO and (Co)Fe$_3$O$_4$–NRGO (900 °C), suggesting a low concentration of Co ions in the samples (Fig. S6D†).

Characterization of FeCo(OH)$_x$ nanosheets

Our unique synthesis method is presented for the fabrication of FeCo(OH)$_x$ nanoparticles (approximately 5 nm) grown directly onto NRGO. These FeCo(OH)$_x$ precursors successfully transformed into well-dispersed (Co)Fe$_3$O$_4$ nanoparticles with an average size of 20.1 nm during calcination. To gain a deeper understanding of the FeCo(OH)$_x$ precursor structure and its transformation mechanism, further characterization techniques are warranted based on our previous studies.

Fig. 3A presents the thermogravimetric analysis (TGA) curves of the FeCo(OH)$_x$–NRGO and Fe(OH)$_x$–NRGO composites at temperatures between 50 °C and 900 °C. The Fe(OH)$_x$–NRGO sample underwent a rapid weight loss at temperatures between 220 °C and 290 °C, likely because of the decomposition of layered hydroxide structures.[1] This aligns with our previous observations of a rapid weight loss at approximately 200 °C associated with the collapse of hydroxide layers in thick-β-Co(OH)$_2$, releasing water molecules.[1] In contrast, single-layered Co(OH)$_2$ on RGO had a relatively high decomposition temperature because there was no layer collapse. Compared with Fe(OH)$_x$, which likely formed thick particles in Fe(OH)$_x$–NRGO, FeCo(OH)$_x$ showed a nanosheet behavior in FeCo(OH)$_x$–NRGO, as shown in the TGA curve. The TEM inspection strongly evidenced the thin-plate structure of FeCo(OH)$_x$ (Fig. 3B and C) prepared under specific solvothermal conditions without the NRGO support. This indicates the presence of few hydroxide layers in FeCo(OH)$_x$, leading to smaller (Co)Fe$_3$O$_4$ nanoparticles compared with the large α-Fe$_2$O$_3$ particles obtained from the Fe(OH)$_x$ particles on NRGO.

Compared with FeCl$_2$ alone, which produced Fe(OH)$_x$ and large α-Fe$_2$O$_3$ aggregates, the addition of CoCl$_2$ in FeCl$_2$ produced a transparent and red colloid without a significant aggregation (Fig. 3B). Further examination using HR-TEM revealed diffraction patterns reminiscent of the (012) and (018) peaks, akin to the LDH structure composed of Co^{2+}–Fe^{3+} (Fig. S7A and B†).[28,29] We suggest that the presence of Co^{2+} might induce the formation of a Co^{2+}–Fe^{3+} LDH nanosheet, leading to tight binding on a two-dimensional NRGO layer. The presence of weakly layered regions within the Co^{2+}–Fe^{3+} LDH nanosheet accounted for the diffraction peaks observed at (012) and (018), indicating preferential diffraction from these crystallographic planes.[28] Furthermore, the EDS mapping demonstrates the overlapping regions of Fe and Co (Fig. S7C†).

Contribution of Co^{2+} in FeCo(OH)$_x$ nanosheets

To elucidate the relationship between the Co^{2+} and Fe^{2+} precursors in this reaction, we investigated the actual atomic ratio by inductively coupled plasma atomic emission spectroscopy and compared it with the expected ratio based on the solvothermal reaction. Interestingly, abnormal behavior was observed when the experimental Co/Fe ratio (Co$_{\text{exp}}$/Fe$_{\text{exp}}$) ranged from 0.5 to 1. This deviated from the anticipated trend. When the Co$_{\text{exp}}$/Fe$_{\text{exp}}$ ratio reached 0.5, the findings supported prior research indicating the substantial influence of the Co^{2+} ions on the formation of the spinel (Co)Fe$_3$O$_4$ form. Additionally, a high Fe content encouraged the development of bulk Fe(OH)$_3$ particles, resulting in the aggregation of the α-Fe$_2$O$_3$ phase (Fig. 1A and S8†). The optimal experimental ratio of Co to Fe precursors (Co$_{\text{exp}}$/Fe$_{\text{exp}}$) was 0.5, resulting in an actual Fe : Co ratio of 2.75 : 0.25. At this ratio, XRD analysis confirmed the successful incorporation of Co into Fe$_3$O$_4$, as expected (Fig. S8A,† shown as a 2 : 1 ratio). However, when the Co$_{\text{exp}}$/Fe$_{\text{exp}}$ ratio was reduced to 0.2 (corresponding to an actual Fe : Co ratio of 2.56 : 0.44), α-Fe$_2$O$_3$ was also observed in the XRD pattern (Fig. S8A,† shown as 2.5 : 0.5). This suggested that a low Co content enables the fast conversion of Fe(OH)$_x$ into α-Fe$_2$O$_3$, whereas a high Co content favors the formation of spinel (Co)Fe$_3$O$_4$, albeit at a relatively low rate. In contrast, when the Co ratio exceeded 1, it fostered the autonomous formation of Co$_3$O$_4$, as evidenced by the XRD pattern at a ratio of 1.5 : 1.5 (Fig. S8†). Without the Fe ions (using only Co ions), small quantities of Co$_3$O$_4$ were formed, as evidenced by a weak and slightly diffracted peak at 36.7° (311) in the XRD pattern (Fig. S8†), which was not prominent on the NRGO in the HR-TEM images (Fig S9†).

This is likely due to the limited oxidation of Co^{2+} ions in our solvothermal system. For the (Co)Fe$_3$O$_4$–NRGO samples, the slight shift of the (311) diffraction peaks toward lower angles supported the substitution of large Co^{2+} ions (radius = 0.69 Å) compared with Fe^{3+} with high spin (radius = 0.60 Å) in the

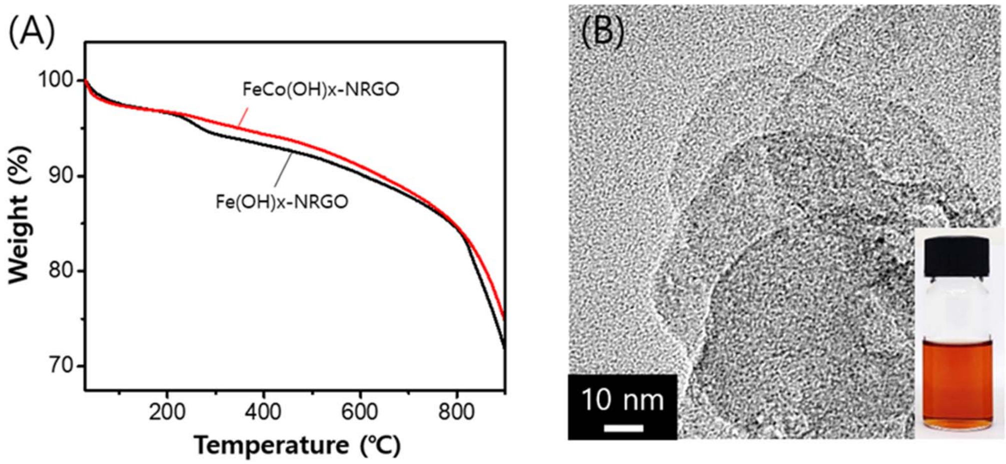

Fig. 3 (A) TGA curves of FeCo(OH)$_x$–NRGO and Fe(OH)$_x$–NRGO under a N$_2$ atmosphere, along with (B) TEM images of the products obtained after a 6 hour solvothermal reaction at 120 °C using only metal precursors (FeCl$_2$ and CoCl$_2$ in a 2 : 1 ratio) and formamide without NRGO (inset: photographs of FeCo(OH)$_x$ solutions after different solvothermal reaction times).

spinel structure. Upon examining the reaction time dependence, it was observed that the Co content peaked at 6 h in the solvothermal reaction. This implied that the contribution of Co gradually increased during synthesis, reaching its peak at 6 h. Beyond this point, it was believed that the contribution of the Fe ions became increasingly prominent as Prussian blue formed, resulting from the decomposition of the solvent formamide and its reaction with the Fe ions.

Additionally, XPS analysis (Fig. S6†) reveals a 0.3 eV positive shift in the Fe^{3+} peak, from 711.2 eV in FeO_x–NRGO(900) to 711.5 eV in (Co)Fe_3O_4–NRGO(900). This suggests modifications in Fe^{3+} within the Fe oxide particles of (Co)Fe_3O_4–NRGO(900). This positive shift of Fe^{3+} upon doping with other transition metals aligns with previous studies, as seen in the Cr-doped Fe_3O_4 procedure published by Chen and co-workers.[30] This claim is further supported by the XRD pattern in Fig. S8B,† which suggests the substitution of some Fe^{3+} ions with Co^{2+} ions due to their similar ionic radii.[4,9] Therefore, the Co incorporation gave better ORR performance than FeO_x–NRGO(900).

ORR activity of (Co)Fe_3O_4–NRGO(900)

The ORR activity of (Co)Fe_3O_4–NRGO(900) was investigated using cyclic voltammetry (CV), linear sweep voltammetry (LSV), and chronoamperometry with a rotating disk electrode (Fig. 5, S10 and 11†). Identical quantities of the samples were deposited onto glassy carbon electrodes for the electrochemical experiments. The CV measurements in O_2-saturated and N_2-saturated 0.1 M KOH electrolytes revealed the electrocatalytic activity for the ORR (Fig. 5A and S10A†). In contrast, (Co)Fe_3O_4–NRGO(900) exhibited a more positive and well-defined ORR peak at 0.87 V *vs.* RHE, indicating a higher half-cell potential and potentially superior ORR activity compared with those of FeO_x–NRGO(900) and its counterparts incorporating (Mn, Ni, and Zn)FeO_x–NRGO(900) (Fig. 5A and S10A†). The relatively broad and less intense ORR peak observed for FeO_x–NRGO(900) at 0.80 V *vs.* RHE can be attributed to the low conductivity of the α-Fe_2O_3 phase (Fig. 1A and B). Fig. 5B and S10B† display the ORR polarization curves obtained by subtracting the N_2-saturated background from the corresponding CV curves. The onset potential and half-wave potential are crucial indicators of the ORR catalytic activity (Table S1†). As expected, (Co)Fe_3O_4–NRGO(900) exhibited a more positive onset potential (0.95 V *vs.* RHE) and half-wave potential (0.86 V *vs.* RHE) than FeO_x–NRGO(900), other metal-incorporated FeO_x–NRGO (Mn, Ni, and Zn), and bare NRGO(900). For (Co)Fe_3O_4–NRGO(900), a region characterized by mixed kinetic and diffusion control was observed between 1.0 and 0.7 V *versus* RHE, followed by a region mainly limited by oxygen transport, as evidenced by the increase in current with higher electrode rotation rates (Fig. S11†). Conversely, FeO_x–NRGO(900) displayed significantly low ORR activity due to the presence of ORR inactive phases, likely including α-Fe_2O_3 (Fig. 5A–D and S2D–F†). In comparison, commercial Pt/C exhibited a mixed kinetic and diffusion-controlled region at higher electrode rotation rates (Fig. S12†).

Fig. 5D presents bar charts comparing the ORR activity, as determined from the LSV curves (Fig. 5B and S10B†), of (Co)Fe_3O_4–NRGO(900) on a glassy carbon electrode to those of bare NRGO(900), FeO_x–NRGO(900), other metal-incorporated FeO_x–NRGO catalysts (Mn, Ni, and Zn), and commercial Pt/C (20 wt% Pt). The specific metrics evaluated included current density at 0.75 V *vs.* RHE and potential at a current density of 2.5 mA cm^{-2} (Co)Fe_3O_4–NRGO(900) exhibited a potential of 0.87 V *vs.* RHE at 2.5 mA cm^{-2} and a current density of 5.01 mA cm^{-2} at 0.75 V *vs.* RHE. These values were comparable to the 0.88 V potential and 5.16 mA cm^{-2} current density observed for commercial Pt/C, demonstrating comparable ORR performance (Fig. 5D).

Beyond Co, this work investigated the influence of other dopant elements (Mn, Ni, and Zn) on ORR activity in our intermediate control approach. While the SEM images shown in Fig.

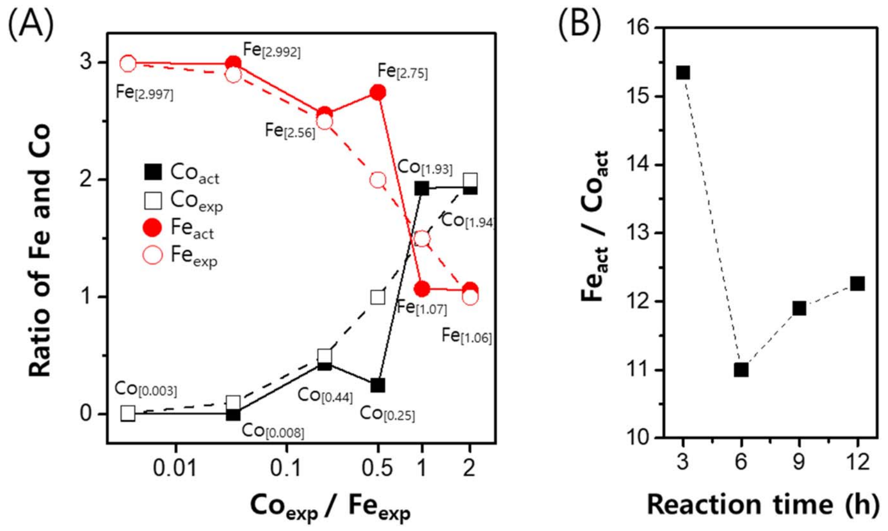

Fig. 4 (A) Comparison of the expected atomic ratios of Fe and Co, derived from the reactant precursors, with the actual atomic ratios (shown in square brackets) determined by ICP-AES. (B) Actual atomic ratios obtained at different solvothermal reaction times for a Co_{exp}/Fe_{exp} feed ratio of 0.5.

S13B† confirm the formation of well-crystallized particles on NRGO for (Mn)FeO_x–NRGO(900), its ORR performance deviates from that of (Co)Fe_3O_4–NRGO(900). (Mn)FeO_x–NRGO(900) exhibited a potential of 0.84 V *vs.* RHE at 2.5 mA cm^{-2}, comparable to that of (Co)Fe_3O_4–NRGO(900) (0.87 V *vs.* RHE). However, Mn doping offered a less pronounced enhancement in ORR activity compared with Co (Table S1†). Conversely, (Ni)FeO_x–NRGO(900) displayed inferior ORR activity compared with bare FeO_x–NRGO (Fig. 5A and Table S1†). This suggested minimal to no positive effect of Ni incorporation within the $Fe(OH)_x$ intermediate system. Finally, (Zn)FeO_x–NRGO(900), as shown in Fig. S13F,† exhibits bulk particle formation, rendering it inactive for ORR catalysis. These observations collectively highlight the crucial role of Co incorporation within our intermediate control system for optimizing ORR performance.

$FeCo(OH)_x$–NRGO exhibited a lower ORR potential (0.68 V *vs.* RHE) than (Co)Fe_3O_4–NRGO(900) (0.87 V *vs.* RHE) at 2.5 mA cm^{-2}, likely because of the inherently low electrical conductivity of the hydroxide phase relative to the (Co)Fe_3O_4 nanocrystals dispersed on the NRGO support (Table S1†). The absence of the Fe_3O_4 phase in $FeCo(OH)_x$–NRGO, as confirmed by TEM images (Fig. 2A–C) and TGA analysis (Fig. 4A), directly translates to poor ORR activity, as evidenced by its high onset potential of 0.84 V *vs.* RHE (Fig. S14 and Table S1†). This highlights the critical role of Fe_3O_4 in facilitating efficient oxygen reduction. As shown in Table S1,† these differences are reflected in the significantly higher onset and half-wave potentials observed for $FeCo(OH)_x$–NRGO compared to those of (Co)Fe_3O_4–NRGO(900). To further understand the reaction kinetics, Tafel slope analysis was employed for the ORR process. The Tafel slope is measured in the kinetic-controlled region in the range between 1.0 V and 0.8 V. A low Tafel slope signifies fast electron transfer kinetics and high intrinsic activity. As expected, (Co)Fe_3O_4–NRGO(900) exhibited the lowest Tafel slope (−59 mV dec^{-1}) compared with Pt/C (−81 mV dec^{-1}), FeO_x–NRGO(900) (−103 mV dec^{-1}), (Mn)FeO_x–NRGO(900) (−83 mV dec^{-1}), (Ni)FeO_x–NRGO(900) (−82 mV dec^{-1}), (Zn)FeO_x–NRGO(900) (−160 mV dec^{-1}) and NRGO(900) (−114 mV dec^{-1}). This indicated that (Co)Fe_3O_4–NRGO(900) enabled the fastest ORR. This Tafel slope analysis, coupled with the positive onset potential of (Co)Fe_3O_4–

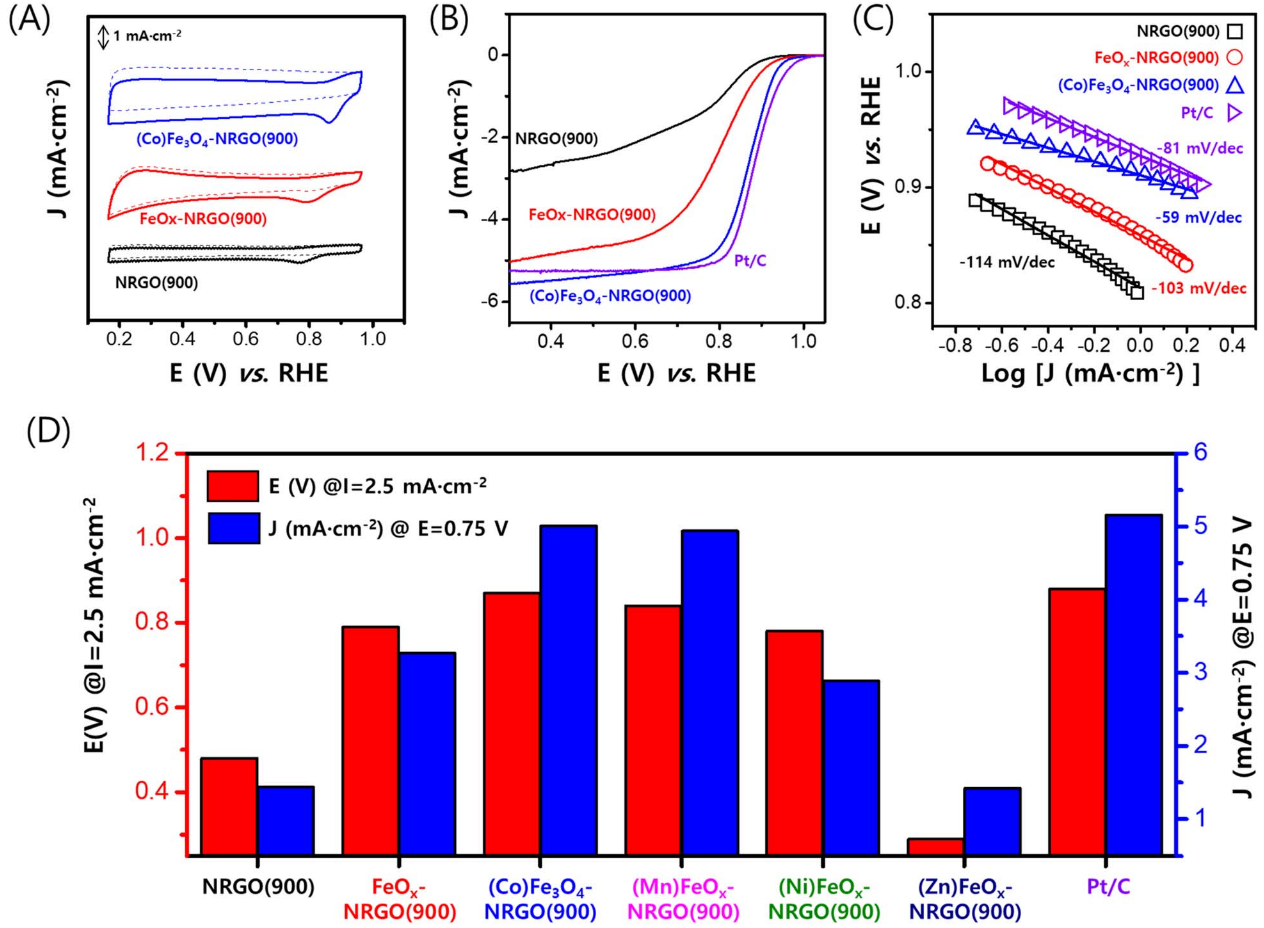

Fig. 5 ORR polarization curves and kinetics of the electrochemical catalysis. (A) CV, (B) LSV curves, and (C) Tafel plots of GC electrodes modified with NRGO(900), FeO_x–NRGO(900) and (Co)Fe_3O_4–NRGO (Mn)FeO_x–NRGO(900), (Ni)FeO_x–NRGO(900), (Zn)FeO_x–NRGO(900), and commercial Pt/C. The ORR kinetics of samples with NRGO(900), FeO_x–NRGO(900), (Co)Fe_3O_4–NRGO and Pt/C are shown in (A)–(C). The CV curves were recorded in 60 mL of 0.1 M KOH electrolyte solution under O_2-saturated conditions (solid line) and N_2-saturated conditions (dashed line) at a scan rate of 25 mV s^{-1}. The LSV curves were recorded in the same electrolyte solution at a scan rate of 5 mV s^{-1} with a rotation rate of 1600 rpm. (D) Bar chart depicting the ORR kinetic current density at 0.75 V *vs.* RHE and the required potentials for $J = 2.5$ mA cm^{-2} for the samples.

NRGO(900), suggested its exceptional potential as a high-performance ORR electrocatalyst (Fig. 5C and S10C†).

Furthermore, our high-temperature calcination (above 900 ° C) successfully produced electrochemically active (Co)Fe_3O_4 nanocrystals on the NRGO layer without significant aggregation or damage to the graphene layers (Fig. 1A, B and 2A–F). This method offers a valuable strategy for synthesizing Fe_3O_4 at high temperatures while suppressing the formation of less active α-Fe_2O_3 (Fig. S4†). Koutecky–Levich (K–L) plots were employed to evaluate the electron transfer number (n) for the ORR process on (Co)Fe_3O_4–NRGO(900) (Fig. S11†).[1,4,9] The electron transfer number of 3.70 for (Co)Fe_3O_4–NRGO(900) supports its exceptional ORR performance, suggesting a near-complete reduction of oxygen to water. Chronoamperometric measurements at 0.75 V *vs.* RHE (Fig. S10D†) revealed the outstanding stability of (Co)Fe_3O_4–NRGO(900). Compared with Pt/C (75% decrease), the (Co)Fe_3O_4–NRGO(900) hybrid exhibited a significantly lower current density decay (42%) over a prolonged 40 000 s test, demonstrating superior long-term stability. Fuel cells can utilize methanol as a fuel through both oxidation and reduction reactions. More importantly, methanol crossover, a major challenge in direct methanol fuel cells (DMFCs), can poison catalysts and hinder performance. Therefore, developing catalysts with high methanol tolerance is critical in DMFCs. We evaluated the methanol tolerance of (Co)Fe_3O_4–NRGO(900) and Pt/C by introducing 1 mL of methanol into an O_2-saturated electrolyte at 200 s (Fig. 6). Notably, the ORR current density of (Co)Fe_3O_4–NRGO(900) remained stable, indicating a negligible impact from methanol. Conversely, Pt/C exhibited a sharp decrease in current, highlighting its susceptibility. This superior methanol tolerance suggests that (Co)Fe_3O_4–NRGO(900) holds promise as a DMFC electrocatalyst. Additionally, to further evaluate the surface poisoning of the catalyst, ORR performance was measured after the addition of 10 mM KSCN to 0.1 M KOH (Fig. S15†). For (Co)Fe_3O_4–NRGO(900), the current density decreased by 13.4% at 0.7 V, while for FeO_x–NRGO(900), it decreased by 73.4% at the same potential. The half-wave potential ($E_{1/2}$) dropped by only 0.04 V for (Co)Fe_3O_4–NRGO(900) (from 0.86 to 0.82 V) but by a larger 0.21 V for FeO_x–NRGO(900) (from 0.91 to 0.70 V). This suggests that the Co ions are uniformly integrated into the Fe_3O_4 lattice, reducing SCN^- adsorption on exposed iron oxide nanoparticles.[31–33]

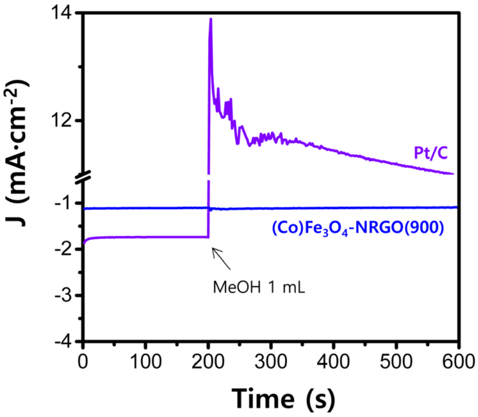

Fig. 6 Chronoamperometric responses for the ORR at 0.75 V *vs.* RHE with a rotation rate of 200 rpm following the addition of 1 mL of methanol (99.9%) for Pt/C and (Co)Fe_3O_4–NRGO(900).

Our results demonstrate that (Co)Fe_3O_4–NRGO(900) exhibits competitive ORR performance and superior stability compared with the commercial Pt/C catalyst. This highlights the effectiveness of our approach, which utilizes the initial formation of nanosized $FeCo(OH)_x$–NRGO and its high-temperature transformation into crystalline, electrochemically active magnetite nanoparticles on NRGO. The high double-layer capacitance of (Co)Fe_3O_4–NRGO(900) likely stems from its large surface area, contributing to its excellent performance. Additionally, it requires low activation energy for charge transportation, further enhancing its practicality. These figures-of-merit compare favourably with those exhibited by Ni catalysts at various calcination temperatures, as well as Ni supported on reduced graphene oxide.[34] At 450 °C, the $E_{1/2}$ value reaches 0.800 V, which is comparable to that of our sample. Notably, unlike many other nanocomposite (N)rGO samples, our sample retains high ORR efficiency even at the critical temperature of 900 °C.

Conclusions

This approach involved the high-temperature calcination of nanosized $FeCo(OH)_2$ nanosheets deposited on NRGO. Both the (Co)Fe_3O_4 nanoparticles and the NRGO support retained excellent quality after high-temperature calcination (900 °C), exhibiting no signs of severe aggregation or breakdown, which is critical for optimal ORR electrocatalysis. Interestingly, TGA analysis revealed the presence of CoFe LDH nanosheets as the initial species deposited on NRGO. This transformation facilitated their efficient decomposition into well-dispersed Co(Fe_3O_4) nanoparticles at high temperatures. The presence of Co^{2+} in this system played a crucial role in the formation of the LDH nanosheet phase. It prevented the formation of less-active α-Fe_2O_3 by promoting the rapid oxidation of iron hydroxide precursors. Our approach offers a simple and effective method for decorating NRGO with electrochemically active magnetite nanoparticles. The intimate interaction between the Co-doped Fe_3O_4 nanocrystals and the porous NRGO support, likely due to covalent coupling, significantly enhanced the catalyst's ORR performance. This is evident from the low onset potential of 0.95 V *vs.* RHE, the high electron transfer number of 3.7, and superior stability compared with those of commercial Pt/C. This method, applicable to various layered metal hydroxide precursors, holds promise for the development of improved ORR catalysts supported on graphene-based materials.

Experimental

Detailed experimental procedures can be found in Section S1 of the ESI.†

Data availability

The data supporting this article have been included as part of the ESI.†

Conflicts of interest

There are no conflicts to declare.

Acknowledgements

This work was supported by the National Research Foundation of Korea (NRF) grant funded by the Korea government (MSIT) (RS-2024-00341027 and RS-2024-00343195) and the Research Fund-2023 of the Catholic University of Korea.

References

1 S. Kwon, H. T. Lee and J. H. Lee, *Chem.–Eur. J.*, 2020, **26**, 14359–14365.
2 C. Wan, X. Duan and Y. Huang, *Adv. Energy Mater.*, 2020, **10**, 1903815.
3 S. Kwon, H. E. Lee, D. Han and J. H. Lee, *ChemComm*, 2021, **57**, 3595–3598.
4 S. Kwon and J. H. Lee, *Bull. Korean Chem. Soc.*, 2021, **42**, 786–791.
5 Y. Jia, Z. Xue, J. Yang, Q. Liu, J. Xian, Y. Zhong, Y. Sun, X. Zhang, Q. Liu and D. Yao, *Angew. Chem., Int. Ed.*, 2022, **61**, e202110838.
6 E. Luo, Y. Chu, J. Liu, Z. Shi, S. Zhu, L. Gong, J. Ge, C. H. Choi, C. Liu and W. Xing, *Energy Environ. Sci.*, 2021, **14**, 2158–2185.
7 K. Liu, J. Fu, Y. Lin, T. Luo, G. Ni, H. Li, Z. Lin and M. Liu, *Nat. Commun.*, 2022, **13**, 2075.
8 J. Liu, X. Wan, S. Liu, X. Liu, L. Zheng, R. Yu and J. Shui, *Adv. Mater.*, 2021, **33**, 2103600.
9 S. Kwon and J. H. Lee, *Dalton Trans.*, 2020, **49**, 1652–1659.
10 E. F. Holby, G. Wang and P. Zelenay, *ACS Catal.*, 2020, **10**, 14527–14539.
11 T. Wang, A. Chutia, D. J. Brett, P. R. Shearing, G. He, G. Chai and I. P. Parkin, *Energy Environ. Sci.*, 2021, **14**, 2639–2669.
12 T. Palaniselvam, V. Kashyap, S. N. Bhange, J. B. Baek and S. Kurungot, *Adv. Funct. Mater.*, 2016, **26**, 2150–2162.
13 Z. Xu, S. Wang, W. Tu, L. Shen, L. Wu, S. Xu, H. Zhang, H. Pan and X. Y. Yang, *Small*, 2024, 2401730.
14 Y. Li, B. Jia, Y. Fan, K. Zhu, G. Li and C. Y. Su, *Adv. Energy Mater.*, 2018, **8**, 1702048.
15 Q. Liu, B. Yu, X. Liao and Y. Zhao, *Energy Environ. Mater.*, 2021, **4**, 407–412.
16 L. Belles, C. Moularas, S. Smykała and Y. Deligiannakis, *Nanomater.*, 2021, **11**, 925.
17 M. Wei, Y. Han, Y. Liu, B. Su, H. Yang and Z. Lei, *J. Alloys Compd.*, 2020, **831**, 154702.
18 M. Liu, Y. Ye, J. Ye, T. Gao, D. Wang, G. Chen and Z. Song, *Magnetochemistry*, 2023, **9**, 110.
19 B. Chutia and P. Bharali, *Catal. Commun.*, 2022, **164**, 106432.
20 J. He, B. Li, J. Mao, Y. Liang, X. Yang, Z. Cui, S. Zhu and Z. Li, *J. Mater. Sci.*, 2017, **52**, 10938–10947.
21 S. Gao, B. Fan, R. Feng, C. Ye, X. Wei, J. Liu and X. Bu, *Nano Energy*, 2017, **40**, 462–470.
22 Z.-S. Wu, S. Yang, Y. Sun, K. Parvez, X. Feng and K. Müllen, *J. Am. Chem. Soc.*, 2012, **134**, 9082–9085.
23 M. M. Ba-Abbad, A. Benamour, D. Ewis, A. W. Mohammad and E. Mahmoudi, *JOM*, 2022, **74**, 3531–3539.
24 P. Khramtsov, M. Kropaneva, D. Kiselkov, A. Minin, L. Chekanova and M. Rayev, *Colloids Surf., A*, 2024, **686**, 133446.
25 M. Su, C. He and K. Shih, *Ceram. Int.*, 2016, **42**, 14793–14804.
26 S. Guo, S. Zhang, L. Wu and S. Sun, *Angew. Chem., Int. Ed.*, 2012, **51**, 11770–11773.
27 S. K. Tiwari, S. Sahoo, N. Wang and A. Huczko, *J. Sci.: Adv. Mater. Devices*, 2020, **5**, 10–29.
28 Q. Abbas, P. A. Shinde, M. A. Abdelkareem, A. H. Alami, M. Mirzaeian, A. Yadav and A. G. Olabi, *Materials*, 2022, **15**, 7804.
29 J.-H. Lee, D. O'Hare and D.-Y. Jung, *Bull. Korean Chem. Soc.*, 2012, **33**, 725–727.
30 S. Meng, S. Sun, Y. Liu, Y. Lu and M. Chen, *J. Colloid Interface Sci.*, 2022, **624**, 433–442.
31 M. Arif, G. Yasin, M. Shakeel, M. A. Mushtaq, W. Ye, X. Fang, S. Ji and D. Yan, *Mater. Chem. Front.*, 2019, **3**, 520–531.
32 S. Hu, W. Ni, D. Yang, C. Ma, J. Zhang, J. Duan, Y. Gao and S. Zhang, *Carbon*, 2020, **162**, 245–255.
33 J. Li, P. Liu, J. Mao, J. Yan and W. Song, *Nanoscale*, 2022, **14**, 6126–6132.
34 Y. Wang, J. Qian, J. Li, J. Xing and L. Liu, *Nanomaterials*, 2023, **13**, 3087.